

## Meander formation in supraglacial streams

Leif Karlstrom,<sup>1</sup> Parmesh Gajjar,<sup>2</sup> and Michael Manga<sup>3</sup>

Received 7 February 2013; revised 10 August 2013; accepted 17 August 2013.

[1] Meandering streams on the surface of glaciers are similar in planform geometry to meanders in alluvial and bedrock rivers, despite fundamental differences in the mechanisms and timescales of incision. We develop depth-averaged conservation equations for flow in such supraglacial channels with erodible boundaries and solve the linear stability problem for harmonic perturbations to an initially straight channel. Meander formation in supraglacial streams is driven by channel curvature, which enhances heat production and heat transfer to the surrounding ice at bend apexes. This leads to enhanced melting and lateral channel migration, with near constant channel width maintained by the competition of lateral erosion and broadscale ablation of the glacier surface. We find that meandering occurs for a wide but finite range of hydraulic and thermal parameters in both subcritical and supercritical flows and that meanders usually propagate downstream. Predicted meander wavelengths are in general agreement with an empirical scaling between supraglacial channel width and meander wavelength derived from glacial environments worldwide.

**Citation:** Karlstrom, L., P. Gajjar, and M. Manga (2013), Meander formation in supraglacial streams, *J. Geophys. Res. Earth Surf.*, 118, doi:10.1002/jgrf.20135.

### 1. Introduction

[2] Supraglacial streams are melt channels that form in the ablation zone of glaciers and ice sheets during the summer season when surface meltwater (sometimes augmented by rainwater) thermally erodes channels into the glacier's surface. These streams form networks that drain off the glacier, most often into supraglacial lakes, moulins, or crevasses. They thus form a primary link between surface, englacial, and subglacial hydrologic systems [*Fountain and Walder*, 1998]. Although there is likely to be some inheritance of large channels from year to year, supraglacial hydrology re-evolves from initial channelization to large-scale organization each year as surface melting waxes and wanes. Over the glacier as a whole, albedo changes caused by such meltwater channelization help set the fine structure of glacial surface ablation, a positive feedback between channelization and melting.

[3] Supraglacial streams are mechanistically distinct from alluvial or bedrock rivers, where mechanical erosion forms the principle mode of incision and channel slope regularization that occurs over much longer timescales [e.g., *Sklar*

and *Dietrich*, 2004]. Yet despite the dominance of thermal erosion, differences in substrate strength and a lack of significant suspended sediment, supraglacial streams exhibit similar qualitative morphologic features such as meandering (including cutoff loops), anastomosing channels, and propagating knickpoints [*Knighton*, 1981; *Marston*, 1983]. Understanding the morphodynamics of these streams thus informs in a broader sense the study of sinuous channels on other terrestrial planets, where potential thermally (or chemically) eroded channels are observed but the substrate characteristics, melt composition, and volumes are often poorly constrained.

[4] This study focuses on meanders because of their ubiquity in supraglacial channels (Figure 1) and utilizes techniques developed to study meandering in alluvial settings [*Seminara*, 2006]. We develop a model for flow in curved channels with fixed cross-sectional geometry and then perform a linear analysis of depth-integrated mass, momentum, and energy conservation equations for harmonic perturbations to flow variables and channel boundaries. This work generalizes previous modeling of *Parker* [1975], following a more general approach taken in recent meandering models of alluvial rivers [e.g., *Blondeaux and Seminara*, 1985; *Camporeale et al.*, 2007]. We end by comparing our model predictions to a compilation of supraglacial stream data from the literature and our own field work.

### 2. Meander Formation

[5] In alluvial settings, variations in boundary shear stresses that exceed the threshold for sediment motion drive bank erosion and deposition. In supraglacial streams, there is no similar mechanism for deposition of bank material (bank

<sup>1</sup>Department of Geophysics, Stanford University, Stanford, California, USA.

<sup>2</sup>School of Mathematics and Manchester Centre for Nonlinear Dynamics, University of Manchester, Manchester, UK.

<sup>3</sup>Department of Earth and Planetary Science, University of California, Berkeley, California, USA.

Corresponding author: L. Karlstrom, Department of Geophysics, Stanford University, 397 Panama Mall, Stanford, CA 94404, USA. (leifk1@stanford.edu)

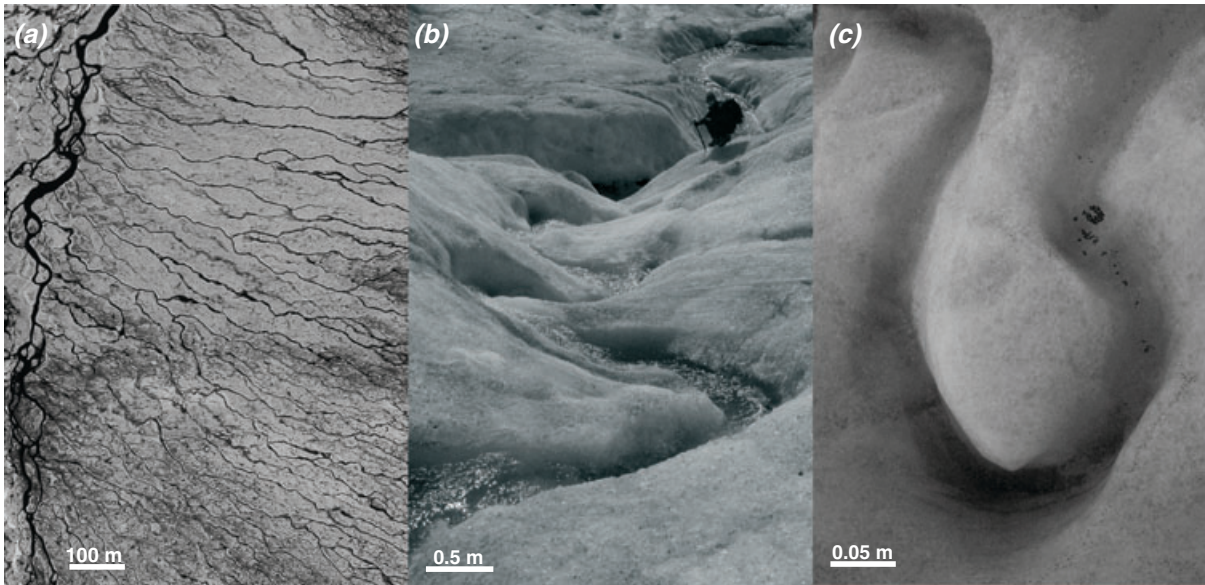


**Figure 1.** (a) Supraglacial stream network on the west Greenland ice sheet, from the near-infrared band of the IKONOS satellite. Image courtesy of Jason Box, Ohio State University, donated by Geoeye to Impossible Pictures UK; (b) Single wavelength meander sequence on the Mendenhall Glacier, Alaska, August 2010, person for scale; (c) Small well-developed meander bend on the Mendenhall Glacier, Alaska, August 2009.

re-freezing is not effective due to long durations of daily solar radiation during the melt season) and generally little sediment (ice or rock) with which to mechanically erode the channel. Meandering supraglacial streams thus exemplify a problem long recognized in bedrock channels [Leopold and Wolman, 1960]: How does channel sinuosity evolve in the absence of bank deposition?

[6] We propose that supraglacial streams migrate through the interaction of two erosional processes: thermal erosion occurring over the entire glacial surface forced by solar radiation and thermal erosion within the channel. Channelized meltwater will attain a higher mean temperature than the surrounding ice due to its lower albedo and the heat dissipated by flow, providing a mechanism to establish long-lived channels that may persist for the duration of the melt season and beyond. A balance between stream incision and large-scale surface lowering will determine the channel geometry. Observations [e.g., Marston, 1983] suggest that in many cases an apparently steady channel cross section is attained, although some channels may continue to cut down until the ice above them creeps and isolates them from the surface [Jarosch and Gudmundsson, 2012].

[7] Melting in supraglacial channels is analogous to sediment transport and mechanical erosion in alluvial settings in that it provides the mechanism by which the channel incises. Melting is, in general, a better understood process than sediment transport, and the stability of melting/solidification fronts is well known [e.g., Mullins and Sekerka, 1963]. Channel sinuosity provides a natural vehicle for streamwise variations in heat transfer as channel bends locally decrease the thickness of the boundary layers separating flowing meltwater and glacial ice, increasing lateral temperature and velocity gradients. This mechanism thus provides a positive feedback that increases frictional dissipation and heat transfer in regions of high channel curvature that leads to

increased thermal erosion. Other sources of spatial variations in heat transfer are possible: for example, anisotropic shielding from solar radiation, nonuniform surface slope, small-scale variations in glacial ice structure and composition, or input/subtraction of water from the system. However, given the ubiquity of meanders in supraglacial streams, we focus on formative mechanisms that do not depend on the particulars of external forcing.

[8] Parker [1975] developed a model for supraglacial stream meanders based on a linear stability analysis of a vertically integrated heat balance, assuming potential flow in an initially straight stream channel. Harmonic perturbations to the bed of the stream were found to be unstable, with a finite range of unstable wave numbers. In particular, Parker [1975] predicts that supercritical flow (Froude number  $Fr > 1$ ) is a necessary condition for meander formation.

[9] Parker's approach is conceptually similar to "bar" models of alluvial meandering [Callander, 1969]: The modeled channel axis remains fixed, but it is assumed that small amplitude perturbations of the bed force eventual lateral channel migration. However, it has since been shown for alluvial rivers that flow perturbations due to curvature in the channel axis are largely responsible for the primary lateral instability, which is reinforced by bed perturbations in the form of point bars and overdeepenings [Ikeda et al., 1981; Blondeaux and Seminara, 1985; Johannesson and Parker, 1989]. We are interested in applying this more general treatment of meandering to the linear stability of supraglacial streams.

### 3. Model

[10] To address the planform evolution of supraglacial channels, we model both the flow within a supraglacial stream and the substrate melting that drives lateral migration

of the channel bank. Because the timescale for water advection is much shorter than the timescale for melting, flow is effectively steady on bank migration timescales. Spatially variable heat transfer occurs as a result of this flow field, which then drives bank melting and migration.

[11] We do not attempt to construct a complete description of supraglacial meltwater routing and note here several important assumptions in our model. We utilize depth-averaged, linearized governing equations, studying the initial perturbations to straight channel geometry rather than finite amplitude effects. We assume constant channel width and neglect vertical structure within the flow. We neglect the time variation of solar forcing (diurnal and seasonal), and the total surface energy balance that provides a temporarily and spatially varying meltwater flux to channels. We also neglect the variations in channel slope that often occur over the length of a supraglacial stream, and hence develop a local model in which these parameters are fixed. Our work is a parameter-sensitivity test that aims to identify a physical mechanism for the onset of meander instabilities, rather than a study of broader-scale channel sinuosity development. In what follows, symbols are defined in the text, with a complete list of variables and parameter ranges in Tables 1 and 2.

### 3.1. Flow in Meandering Coordinates

[12] We now develop a model for the flow field in supraglacial streams, using meandering coordinates to express the appropriate conservation equations in a translating coordinate system that tracks the channel centerline described by coordinates  $(X_0^*(s^*), Y_0^*(s^*), Z_0^*)$  (Figure 2). This coordinate system, in which  $s^*$  and  $n^*$  represent downstream and cross-stream positions (asterisks indicate dimensional

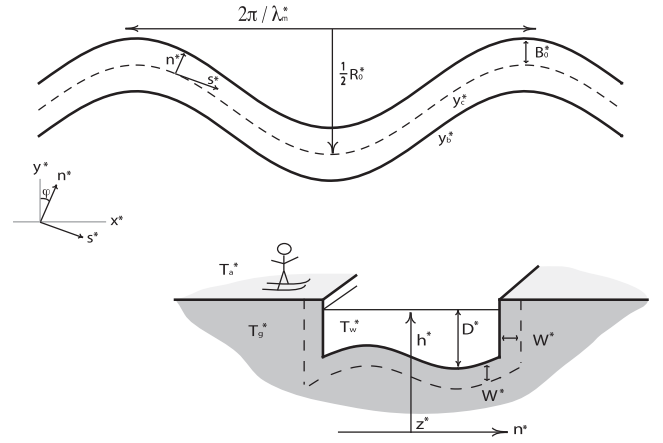


**Figure 2.** Model geometry and coordinate system definition.

variables), is mapped to a fixed cartesian basis  $(X^*, Y^*, Z^*)$  via

$$(X^*, Y^*, Z^*) = (X_0^* + n^* \sin \phi, Y_0^* + n^* \cos \phi, Z^*), \quad (1)$$

from which we obtain the metric coefficients

$$(h_s^*, h_n^*, h_z^*) = (1 + n^* \kappa^*(s^*), 1, 1), \quad (2)$$

where  $\kappa^*(s^*) = d\phi/ds^*$  is the curvature of the channel centerline. The angle of the centerline from the  $X^*$  axis is  $\phi$ , and the slope of the channel axis is assumed to be small. More details about the derivation of this coordinate system and the resulting curvilinear differential operators may be found in the alluvial meander literature, for example, *Seminara and Tubino* [1992]. The radius of curvature scales with its typical length scale  $R_0^*$  as  $1/\kappa^* = R_0^*/\kappa$ .

### 3.2. Governing Equations for Flow

[13] In the meandering coordinate system, flow variables scale as

$$(s, n) = \frac{(s^*, n^*)}{B_0^*}, \mathbf{v} = (u, v, w) = \frac{(u^*, v^*, w^*)}{U_0^*}, (h, D, z) = \frac{(h^*, D^*, z^*)}{D_0^*}, \quad (3)$$

where  $(u, v, w)$  are components of the velocity vector  $\mathbf{v}$  taking characteristic value  $U_0^*$ , and  $(h, D, z)$  are the water surface height, water depth, and height above a datum, respectively (Figure 2), that all scale with the characteristic depth  $D_0^*$ .  $B_0^*$  is the channel half width. The Reynolds equations for momentum and mass conservation are

$$\begin{aligned} N \frac{\partial}{\partial s} (u^2) + \frac{\partial}{\partial n} (uv) + \beta \frac{\partial}{\partial z} (uw) + 2\nu_0 N k u v \\ = -\frac{N}{Fr^2} \frac{\partial h}{\partial s} + \beta \sqrt{C_f} \frac{\partial}{\partial z} \left( \nu_T \frac{\partial u}{\partial z} \right), \\ N \frac{\partial}{\partial s} (uv) + \frac{\partial}{\partial n} (v^2) + \beta \frac{\partial}{\partial z} (vw) + \nu_0 N k (v^2 - u^2) \\ = -\frac{1}{Fr^2} \frac{\partial h}{\partial n} + \beta \sqrt{C_f} \frac{\partial}{\partial z} \left( \nu_T \frac{\partial v}{\partial z} \right), \\ N \frac{\partial u}{\partial s} + \left( \frac{\partial}{\partial n} + \nu_0 N k \right) v + \beta \frac{\partial w}{\partial z} = 0, \end{aligned} \quad (4)$$

**Table 1.** Model Variables

Variable	Description	Units
$s^*, n^*$	Downstream, cross-stream coordinates	m
$X^*, Y^*$	Cartesian coordinates	m
$z^*$	Depth coordinate	m
$S^*$	Glacier surface height	m
$\lambda_m^*$	Bank perturbation wave number	1/m
$k^*$	Flow perturbation wave number	1/m
$\omega^*$	Perturbation frequency	1/s
$\kappa^*$	Stream radius of curvature	1/m
$N$	Metric coefficient	–
$t^*$	Time	s
$u^*, U^*$	Downstream velocity	m/s
$v^*, V^*$	Cross-stream velocity	m/s
$w$	Vertical stream velocity	m/s
$\mathcal{A}_1, \mathcal{B}_1, \mathcal{D}_1, \mathcal{H}_1$	Perturbation amplitudes	–
$U^*$	Water speed	m/s
$d^*, D^*$	Channel depth	m
$h^*, H^*$	Water surface height	m
$y_b^*, y_c^*$	Channel bank, channel centerline	m
$W^*$	Ice thermal boundary layer	m
$T^*$	Water temperature	°C
$\Gamma_T^*$	Turbulent diffusivity of heat	m <sup>2</sup> /s
$\nu_T^*$	Turbulent diffusivity of momentum	m <sup>2</sup> /s
$a^*$	Viscous dissipation	W/m <sup>2</sup>
$\sigma_s^*, \sigma_n^*$	Wall shear stress	Pa
$\ell^*$	Lateral boundary layer in stream	m
$\varepsilon$	Expansion parameter	–
$C_f$	Wall friction	–

**Table 2.** Model Parameters With the Range of Values Considered

Parameter	Description	Range	Units
$B_0^*$	Channel half width	[0.1, 1]	m
$D_0^*$	Channel scale depth	[0.05, 0.5]	m
$U_0^*$	Scale velocity	[0.25, 2.5]	m/s
$R_0^*$	Scale radius of curvature	–	1/m
$\tau^*$	Scale time	–	s
$L^*$	Latent heat of fusion	334	kJ/kg
$\rho^*$	Ice/water density	1000	kg/m <sup>3</sup>
$g^*$	Gravitational constant	9.81	m/s <sup>2</sup>
$\gamma^*$	Solar forcing constant	[10, 50]	W/m <sup>2</sup> K
$k_T^*$	Ice thermal conductivity	2	W/m <sup>2</sup> K
$\alpha$	Exponent, boundary layer scaling	0.5	–
$\mu^*$	Water kinematic viscosity	10 <sup>-6</sup>	m <sup>2</sup> /s
$c_p^*$	Specific heat capacity	4200	J/kg K
$\Delta T_a^*$	Temperature difference water and air	10	°C
$\Delta T_G^*$	Temperature difference water and ice	[0.05, 0.5]	°C
$\mathcal{J}^*$	Coupling constant temperature model	[10 <sup>-5</sup> , 10 <sup>-2</sup> ]	s/m
$C^*$	Coupling constant boundary layer	[10 <sup>-1</sup> , 10 <sup>1</sup> ]	W/m <sup>2</sup> K
$C_b$	Proportionality between lateral and vertical melting	[0.25, 4]	–
$\zeta^*$	Wall roughness height	0.001	m
<b>Dimensionless parameters</b>			
$C_0$	Wall friction base state	–	–
$\nu_0$	Ratio half width to radius of curvature	–	–
$\beta$	Ratio half width to depth	–	–
Fr	Froude number	–	–
Ec	Eckert number	–	–
$\Pi_0$	Ratio of melting to dissipation	–	–
$\Pi_1$	Ratio of advection to dissipation	–	–
$\Pi_2$	Ratio of conduction to dissipation	–	–
$\Pi_3$	Ratio of solar forcing to dissipation	–	–
$\Pi_4$	Ratio of lateral heat transfer to dissipation	–	–

where  $N = (1 + \nu_0 n \kappa)^{-1}$  is the longitudinal metric coefficient of the coordinate system with  $\nu_0 = B_0^*/R_0^*$ ,  $\beta = B_0^*/D_0^*$  is the half width to depth ratio,  $Fr = U_0^*/\sqrt{g^* D_0^*}$ , is the Froude number,  $C_f$  is a dimensionless friction coefficient, while  $\nu_T = \nu_T^*/(C_f^{1/2} U_0^* D_0^*)$  is a dimensionless eddy viscosity. Hydrostatic pressure is incorporated into equations (4), while the Reynolds stresses and lateral bed stress have been neglected.

[14] After applying the depth averaging operation  $\langle \cdot \rangle = D^{-1} \int_{h-D}^h (\cdot) dz$ , equations (4) become

$$\begin{aligned}
 NU \frac{\partial U}{\partial s} + V \frac{\partial U}{\partial n} + \nu_0 N \kappa UV + N \frac{\partial H}{\partial s} + \frac{\beta \sigma_s}{D} &= 0, \\
 NU \frac{\partial V}{\partial s} + V \frac{\partial V}{\partial n} - \nu_0 N \kappa U^2 + \frac{\partial H}{\partial n} + \frac{\beta \sigma_n}{D} &= 0, \\
 N \frac{\partial}{\partial s} (DU) + \frac{\partial}{\partial n} (DV) + \nu_0 N \kappa DV &= 0.
 \end{aligned} \tag{5}$$

Here  $U = \langle u \rangle$ ,  $V = \langle v \rangle$  are the depth-averaged velocities and  $H = h/Fr^2$ , while  $\sigma_s, \sigma_n$  are the downstream and cross-stream shear stresses. Equations (5) are identical to those of *Blondeaux and Seminara* [1985], who similarly neglect the vertical structure of the flow. Such an approximate description of the flow is appropriate for channels wider than they are deep, a condition that is generally satisfied by supraglacial streams although we note that channel aspect ratios are generally smaller than their alluvial counterparts.

We also make the common assumption [e.g., *Smith and McLean*, 1984] that depth averages may be decomposed for general variables  $\Psi, \Theta$  as  $\langle \Psi \Theta \rangle \sim \langle \Psi \rangle \langle \Theta \rangle$ .

### 3.3. Heat Transfer

[15] Equations (5) are coupled to the Reynolds-averaged heat equation. We do not attempt a global energy balance which would set the total meltwater production for a given glacial surface lowering, thus, the slope does not enter explicitly into our formulation (slope sets the scale for flow variables). Instead, we use a local energy equation for which the dimensional viscous dissipation  $a^*$ , turbulent diffusivity  $\Gamma_T^*$ , and water temperature  $T^*$  scale as

$$a = \frac{D_0^*}{\rho^* U_0^{*3}} a^*, \quad \Gamma_T = \frac{\Gamma_T^*}{U_0^* D_0^*}, \quad T = \frac{T^*}{\Delta T_G^*}, \tag{6}$$

where  $\rho^*$  is water density and  $\Delta T_G^*$  is the bulk temperature difference between the stream water and the glacier ice.

[16] The Reynolds-averaged dimensionless heat equation in meandering coordinates may be written as

$$\nabla \cdot \left( \sqrt{T} - \frac{\Gamma_T}{\beta} \nabla T \right) = Ec \beta a, \tag{7}$$

where  $Ec = U_0^{*2}/c_p^* \Delta T_G^*$  is the Eckert number measuring the relative importance of kinetic energy and enthalpy and  $\Gamma_T$  is a turbulent diffusivity defined in equation (6). We note

that in meandering coordinates the divergence of a vector  $\mathbf{r} = (r_s, r_n, r_z)$  is

$$\nabla \cdot \mathbf{r} = N \frac{\partial r_s}{\partial s} + \nu_0 N \kappa r_n + \frac{\partial r_n}{\partial n} + \beta \frac{\partial r_z}{\partial z}, \quad (8)$$

while the gradient operator is  $\nabla = (N \frac{\partial}{\partial s}, \frac{\partial}{\partial n}, \beta \frac{\partial}{\partial z})$ . Equation (7) utilizes a mixing length model to relate the time average of fluctuating temperature and velocity field to the mean temperature gradient in the flow.

[17] We make the further assumption that mean temperature gradients track velocity gradients via the Reynolds analogy  $\nabla T = \mathcal{J}^* U_0^* \nabla \mathcal{U}$  where the flow speed is  $\mathcal{U} = \sqrt{U^2 + V^2}$ . The empirical and dimensional constant  $\mathcal{J}^*$  measures the strength of coupling between velocity and temperature gradients. For flow past a flat plate with Prandtl number  $Pr$  equal to unity,  $\mathcal{J}^* = 1/U_0^*$  [Schlichting, 1960], but we leave it here as an adjustable parameter.

[18] After applying continuity and modeling  $\Gamma_T = \mathcal{U}D$ , the depth average of equation (7) is

$$\begin{aligned} \frac{\mathcal{J}^* U_0^*}{\beta Ec} \left( NUD \frac{\partial \mathcal{U}}{\partial s} + VD \frac{\partial \mathcal{U}}{\partial n} - \frac{1}{\beta} \left( N \frac{\partial}{\partial s} \left( \mathcal{U} D^2 \frac{\partial \mathcal{U}}{\partial s} \right) \right. \right. \\ \left. \left. + \frac{\partial}{\partial n} \left( \mathcal{U} D^2 \frac{\partial \mathcal{U}}{\partial n} \right) + \nu_0 N \kappa \mathcal{U} D^2 \frac{\partial \mathcal{U}}{\partial n} \right) \right) \\ = \frac{1}{\rho^* U_0^{*3}} (q^*|_{z=h-D} - q^*|_{z=h}) + \langle a \rangle D, \quad (9) \end{aligned}$$

where  $q^*|_{z=h-D}$  is the (dimensional) vertical heat transport in the water at the water-ice interface and  $q^*|_{z=h}$  is the vertical heat transport in the water at the water-air interface. Boundary terms associated with turbulent advection of heat are ignored, and we have simplified the gradient operator in the mixing length model by neglecting terms associated with the meandering coordinate system. These terms drop out in the linearization of equation (9) performed in section 4, so are unnecessary for our study. Equation (9) balances the rate of heat generation by viscous dissipation at the smallest length scales in the stream with heat transport at the top and bottom boundaries, as well as advection by the mean flow.

[19] At the air-water interface, transport of both sensible and latent occurs by a combination of radiation (solar forcing) and advection by wind. We assume that

$$q^*|_{z=h} = -\gamma^* \Delta T_A^*, \quad (10)$$

with  $\Delta T_A^* = T_a^* - T_w^*$  the temperature difference between water and air and  $\gamma^*$  the coefficient of heat transfer at the water-air interface.

[20] Heat transfer at the bottom boundary is normal to the ice-water interface and follows a kinematic Stefan condition for boundary melting

$$\frac{\rho^* L^* D_0^*}{\tau^*} \frac{\partial (h-D)}{\partial t} = q^*|_{z=h-D} - q_I^*, \quad (11)$$

where  $\rho^*$  is the density of ice (assumed equal to the density of water) and  $L^*$  is the latent heat of fusion.

[21] The heat flux through the glacier  $q_I^*$  is modeled by

$$q_I^* = -\frac{k_I^* (T_w^* - T_G^*)}{W^*} = -\frac{k_I^* \Delta T_G^*}{W^*}, \quad (12)$$

where  $T_w^*, T_G^*$  are the mean air and bulk glacier ice temperatures,  $W^*$  is a conductive boundary layer in the ice that scales with the flow depth  $D_0^*$ , and  $k_I^*$  is thermal conductivity.

[22] Because supraglacial stream water is strongly buffered toward  $0^\circ\text{C}$  [Isenko *et al.*, 2005], the water temperature is a good approximation to the ice melting temperature in equation (12). We thus neglect diurnal fluctuations in stream water temperature. In supraglacial streams,  $\Delta T_G^*$  will be a function of latitude and altitude, close to zero in temperate glaciers and larger in polar settings.

[23] The characteristic time for channel lowering is a melting timescale,  $\tau_{\text{melt}}^* = L^* D_0^* / U_0^{*3}$ , which is far greater than the timescale for advection  $\tau_{\text{advect}}^* = B_0^* / U_0^*$ . Thus, the problem of flow in supraglacial streams is largely decoupled from bank and basal melting. However, this balance sets the equilibrium depth of the channel and thus determines the flow field.

[24] Dissipation  $\langle a \rangle$  in the stream is modeled following Parker [1975]:

$$\langle a \rangle = \frac{\sigma_s U + \sigma_n V}{D}, \quad (13)$$

with the near-bed shear stress terms  $(\sigma_s, \sigma_n)$  represented as

$$(\sigma_s, \sigma_n) = \frac{(\sigma_s^*, \sigma_n^*)}{\rho^* U_0^{*2}} = C_f \mathcal{U} (U, V). \quad (14)$$

[25] The friction factor  $C_f$  is given by an empirical approximation for rough-walled pipe flow [Colebrook, 1939; Parker, 1975]:

$$(C_f)^{-1/2} = -2 \log \left( \frac{\zeta^*}{3.7 D^*} + \frac{2.5}{\text{Re} \sqrt{C_f}} \right). \quad (15)$$

The Reynolds number is  $\text{Re} = U_0^* D^* / \mu^*$ , with  $\mu^*$  the water kinematic viscosity and  $\zeta^*$  a characteristic roughness height of the channel walls.

[26] Inserting models (11)–(15) into equation (9) gives the final energy equation, balancing the divergence of heat from the channel cross-section boundary with internal frictional dissipation:

$$\begin{aligned} \Pi_0 \frac{\partial (h-D)}{\partial t} = \Pi_1 \left( NUD \frac{\partial \mathcal{U}}{\partial s} + VD \frac{\partial \mathcal{U}}{\partial n} \right) \\ - \frac{\Pi_1}{\beta} \left( N \frac{\partial}{\partial s} \left( N \mathcal{U} D^2 \frac{\partial \mathcal{U}}{\partial s} \right) + \frac{\partial}{\partial n} \left( \mathcal{U} D^2 \frac{\partial \mathcal{U}}{\partial n} \right) \right. \\ \left. + \nu_0 N \kappa \mathcal{U} D^2 \frac{\partial \mathcal{U}}{\partial n} \right) \\ + \Pi_2 \frac{1}{W} - \Pi_3 - C_f \mu^3. \quad (16) \end{aligned}$$

[27] The dimensionless numbers

$$\begin{aligned} \Pi_0 = \frac{L^* D_0^*}{\tau^* U_0^{*3}}, \quad \Pi_1 = \frac{\mathcal{J}^* c_p^* \Delta T_G^*}{\beta U_0^*}, \\ \Pi_2 = \frac{k_I^* \Delta T_G^*}{D_0^* \rho^* U_0^{*3}}, \quad \Pi_3 = \frac{\gamma_E^* \Delta T_a^*}{\rho^* U_0^{*3}}, \quad (17) \end{aligned}$$

compare dissipation with melting over time ( $\Pi_0$ ), advection of mean temperature ( $\Pi_1$ ), conduction in the ice ( $\Pi_2$ ), and solar forcing ( $\Pi_3$ ). We use the melting timescale  $\tau^* = \tau_{\text{melt}}^* = L D_0^* / U_0^{*3}$  so that  $\Pi_0 = 1$  in what follows. For a range of physical parameter values (Table 2), all the terms that appear on the right-hand side of equation (16) are of similar magnitude.

### 3.4. Lateral Channel Migration and Boundary Conditions

[28] A kinematic (Stefan) condition governs the lateral migration of the channel bank  $y_b^*$  on the melting timescale, normal to the lateral channel boundaries:

$$\rho^* L^* \frac{\partial y_b^*}{\partial t^*} = q_w^* - q_I^* \quad \text{at } n^* \pm B_0^*, \quad (18)$$

where  $q_w^*$  and  $q_I^*$  are the lateral heat fluxes at the ice-water interface through water and ice.

[29] Heat transfer at the bank scales with boundary layer thickness  $\ell^*$ , which depends on flow Reynolds number to some power  $\alpha$  as  $\ell \sim \text{Re}^{-\alpha}$ .

$$q_w^* \sim \frac{\Delta T_G^*}{\ell^*} = C^* \Delta T_G^* \text{Re}^\alpha = C^* \Delta T_G^* \left( \frac{U^* D^*}{\mu^*} \right)^\alpha, \quad (19)$$

with  $C^*$  a dimensional scaling factor.

[30] Heat lost to ice is given by equation (12), but with the opposite sign because of how channel migration is defined. This implies that the thermal boundary layer in glacier ice is similar on the sides and the bottom of the stream. In dimensionless form, the lateral migration condition is

$$\Pi_0 \beta \frac{\partial y_b}{\partial t} = \Pi_4 (\mathcal{U}D)^\alpha - \Pi_2 \frac{1}{W}, \quad (20)$$

where

$$\Pi_4 = \frac{C^* \Delta T_G^* U_0^{*\alpha-3} D_0^{*\alpha}}{\rho^* \mu^{*\alpha}} \quad (21)$$

is a dimensionless ratio of melting and boundary layer heat transfer at the channel walls. We use  $\alpha = 0.5$  for turbulent flow [Schlichting, 1960].

[31] The governing equations (5) and (16) contain four unknown flow variables and are closed with four boundary conditions. We therefore supplement equation (20) with Dirichlet conditions stating that the channel walls are impermeable to flow:

$$V = 0 \quad \text{at } n = \pm 1. \quad (22)$$

[32] Implicit in our model development is the assumption that a steady channel shape is maintained, which requires that large-scale lowering of the glacier surface keeps pace with lateral migration to maintain constant channel width. This assumption is grounded in observations of nearly constant width channels (Figure 2) and is similar to early alluvial meandering studies [Blondeaux and Seminara, 1985; Seminara, 2006] that separate the problem of meander formation from that of channel geometry. In our case this assumption implies that lowering of the channel relative to the glacier surface  $S^*$  [Parker, 1975] (Figure 2) is proportional to the lateral migration of channel bank  $y_b^*$ :

$$\frac{\partial y_b^*}{\partial t^*} = C_b \left( \frac{\partial S^*}{\partial t^*} - \frac{\partial (h^* - D^*)}{\partial t^*} \right), \quad (23)$$

where  $C_b$  is a parameter of order unity. Our problem is thus completely specified, with control parameters  $\Pi_0, \Pi_1, \Pi_2, \Pi_3, \Pi_4, \beta$ , and  $\text{Fr}$ .

### 4. Linear Stability Analysis

[33] We now perform a linear stability analysis on governing equations (5) and (16), in a similar manner to *Blondeaux and Seminara* [1985], where further details may be found. We examine a channel whose centerline exhibits small-amplitude perturbations, a straight base state, and investigate the conditions for these perturbations to grow in time. We make the harmonic perturbation (noting that here and elsewhere the complex conjugate of the perturbations must be added to form a real quantity)

$$\kappa = \frac{1}{R_0} e^{i(\lambda_m s - \omega t)}, \quad (24)$$

where  $\lambda_m$  is a nondimensional meander wave number scaled by the half width  $B_0^*$  and  $\omega$  is a complex frequency that dictates the growth rate as well as propagation direction and speed of harmonic disturbances.

[34] The channel centerline is perturbed as

$$y_c = \varepsilon e^{i(kx - \omega t)}, \quad (25)$$

where  $y_c, \varepsilon, k$ , and  $x$  are quantities normalized by the half width  $B_0^*$  and  $\varepsilon \ll 1$  is a small parameter for the Taylor expansions involved in the linearization.

[35] For this assumption to hold, we must also have

$$v_0 = k^2 \varepsilon, \quad \lambda_m = k + \mathcal{O}(\varepsilon^2 k^2), \quad s = x + \mathcal{O}(\varepsilon^2 k^2). \quad (26)$$

We follow *Blondeaux and Seminara* [1985] in assuming that the flow is fully developed in the  $s$  direction, with no secondary flow. We perturb the flow variables ( $U, V, h, D$ ) as an expansion in  $\varepsilon$ :

$$(U, V, h, D) = (1, 0, h_0, 1) + \varepsilon (\mathcal{A}_1, \mathcal{B}_1, \mathcal{H}_1, \mathcal{D}_1) e^{i(kx - \omega t)} + \mathcal{O}(\varepsilon^2 k^2), \quad (27)$$

where  $\mathcal{A}_1, \mathcal{B}_1, \mathcal{H}_1, \mathcal{D}_1$  are all functions of  $n$  alone and  $h_0$  is the nondimensional unperturbed depth.

[36] The thermal boundary layers in ice surrounding the stream  $W$  are assumed to track perturbations in the flow depth  $D_0$  and channel lateral boundaries, respectively, with base states that scale with the flow depth. These are modeled by

$$W = 1 + \varepsilon \mathcal{D}_1 e^{i(kx - \omega t)} + \mathcal{O}(\varepsilon^2 k^2). \quad (28)$$

Expanding  $C_f$  as a function of  $\mathcal{U}$  and  $D$  in powers of  $\varepsilon$ , we have

$$C_f = C_0 + \varepsilon \frac{\partial C_f}{\partial \mathcal{U}} \frac{\partial \mathcal{U}}{\partial \varepsilon} \Big|_{\varepsilon=0} + \varepsilon \frac{\partial C_f}{\partial D} \frac{\partial D}{\partial \varepsilon} \Big|_{\varepsilon=0} + \mathcal{O}(\varepsilon^2). \quad (29)$$

This gives

$$\begin{aligned} \sigma_s &= C_0 \left( 1 + \varepsilon (s_1 \mathcal{A}_1 + s_2 \mathcal{D}_1) e^{i(\lambda_m s - \omega t)} \right) + \mathcal{O}(\varepsilon^2) \\ \sigma_n &= \varepsilon \mathcal{B}_1 C_0 e^{i(\lambda_m s - \omega t)} + \mathcal{O}(\varepsilon^2) \end{aligned} \quad (30)$$

where

$$s_1 = 2 + \frac{1}{C_0} \frac{\partial C_f}{\partial \mathcal{U}}, \quad s_2 = \frac{1}{C_0} \frac{\partial C_f}{\partial D}. \quad (31)$$

The zeroth-order friction parameter  $C_0$  as well as the derivatives  $\partial C_f / \partial \mathcal{U}$  and  $\partial C_f / \partial D$  may be evaluated in closed form using the principal solution for  $w$  in  $z = we^w$ .

#### 4.1. Solution of the Linearized Problem

[37] Substituting all the expansions into the governing differential system (5) and (16), at  $\mathcal{O}(\varepsilon^0)$ , we find the uniform flow solution and energy balance within the stream:

$$\frac{1}{Fr^2} \frac{dh_0}{ds} = -\beta C_0, \quad (32)$$

$$\Pi_0 \frac{dh_0}{dt} = \Pi_2 - \Pi_3 - C_0 \quad (33)$$

In equation (33), a nonzero right-hand side sets the average lowering rate of the stream relative to glacier surface lowering [Parker, 1975]. Background lowering of the glacier surface enters through  $\Pi_2$  and  $\Pi_3$ , with  $\Pi_3$  measuring net solar radiation. We neglect relative motion between stream lowering and ice surface lowering.

[38] At  $\mathcal{O}(\varepsilon^1)$ , we have

$$\begin{bmatrix} a_1 & \frac{d}{dn} & 0 & a_1 \\ a_2 & 0 & a_3 & a_4 \\ 0 & a_5 & a_6 \frac{d}{dn} & 0 \\ a_7 + a_8 \frac{d^2}{dn^2} & 0 & a_9 & a_{10} \end{bmatrix} \begin{bmatrix} \mathcal{A}_1 \\ \mathcal{B}_1 \\ \mathcal{H}_1 \\ \mathcal{D}_1 \end{bmatrix} = \begin{bmatrix} 0 \\ -n\lambda_m^2 \chi_0 \\ \lambda_m^2 \\ 0 \end{bmatrix}. \quad (34)$$

with  $\chi_0 = \beta C_0$ , and the coefficients  $a_i$  ( $i = 1, 2, \dots, 10$ ) defined by

$$\left. \begin{aligned} a_1 &= i\lambda_m, & a_2 &= i\lambda_m + \chi_0 s_1, \\ a_3 &= \frac{i\lambda_m}{Fr^2}, & a_4 &= \chi_0(s_2 - 1), \\ a_5 &= i\lambda_m + \chi_0, & a_6 &= \frac{1}{Fr^2}, \\ a_7 &= C_0(s_1 + 1) - \Pi_1(i\lambda_m + \lambda_m^2/\beta), \\ a_8 &= \Pi_1/\beta, & a_9 &= -i\omega\Pi_0 \\ a_{10} &= C_0 s_2 + i\omega\Pi_0 + \Pi_2. \end{aligned} \right\} \quad (35)$$

By manipulating this system, we obtain a simpler fourth-order equation in  $\mathcal{B}_1$

$$\Sigma_0 \mathcal{B}_1 + \Sigma_2 \frac{d^2 \mathcal{B}_1}{dn^2} + \Sigma_4 \frac{d^4 \mathcal{B}_1}{dn^4} = \sigma \quad (36)$$

where

$$\Sigma_0 = a_5 \left( a_{10} - a_7 - \frac{(a_4 - a_2)a_9}{a_3} \right), \quad (37)$$

$$\Sigma_2 = -a_5 a_8 + \frac{a_6(a_2 a_{10} - a_7 a_4)}{a_1 a_3}, \quad (38)$$

$$\Sigma_4 = \frac{-a_4 a_6 a_8}{a_1 a_3}, \quad (39)$$

$$\sigma = \lambda_m^2 \left[ (a_{10} - a_7) \left( \frac{a_6 \chi_0}{a_3} + 1 \right) - \frac{a_9}{a_3} (a_4 - a_2) \right]. \quad (40)$$

This is coupled to equations in the other variables. Equation (36) has the form of a forced linear oscillator, which is also characteristic of alluvial meander models [Blondeaux and Seminara, 1985].

[39] With some manipulation, the boundary conditions equations (20) and (22) at  $\mathcal{O}(\varepsilon^1)$  become

$$\frac{d^2 \mathcal{B}_1}{dn^2} = \Gamma \quad \text{at } n = \pm 1, \quad (41)$$

$$\mathcal{B}_1 = 0 \quad \text{at } n = \pm 1, \quad (42)$$

where

$$\Gamma = \frac{a_1 \Pi_2 \lambda_m^2 (a_6 \chi_0 + a_3)}{a_6 (a_2 a_3 \Pi_2 - (a_4 - a_2) \alpha \Pi_4)}. \quad (43)$$

We solve the differential equation (36) with boundary conditions (41) and (42) giving

$$\mathcal{B}_1(n) = \frac{\sigma}{\Sigma_0} + C_1 \cosh(\theta_+ n) + C_2 \cosh(\theta_- n), \quad (44)$$

where

$$\theta_{\pm} = \left( \frac{-\Sigma_2 \pm \sqrt{\Sigma_2^2 - 4\Sigma_0 \Sigma_4}}{2\Sigma_4} \right)^{1/2}, \quad (45)$$

and

$$C_1 = \frac{\Gamma \Sigma_0 + \theta_-^2 \sigma}{\cosh(\theta_+) \Sigma_0 (\theta_+^2 - \theta_-^2)}, \quad (46)$$

$$C_2 = -\frac{\Gamma \Sigma_0 + \theta_+^2 \sigma}{\cosh(\theta_-) \Sigma_0 (\theta_+^2 - \theta_-^2)}. \quad (47)$$

Perturbation amplitudes  $\mathcal{A}_1$ ,  $\mathcal{D}_1$ , and  $\mathcal{H}_1$  follow from substituting equation (44) into (34).

[40] We accept only those perturbations that do not change the discharge of the stream and the overall surface slope. These are expressed at linear order through the following integral conditions:

$$\int_{n=-1}^{n=1} \mathcal{A}_1(n) + \mathcal{D}_1(n) dn = 0, \quad (48)$$

$$\int_{n=-1}^{n=1} \mathcal{H}_1(n) - \mathcal{D}_1(n) dn = 0, \quad (49)$$

which state that perturbations to the flow field do not affect the overall discharge and surface slope, respectively.  $\mathcal{A}_1$ ,  $\mathcal{H}_1$ , and  $\mathcal{D}_1$  are all odd functions of  $n$  and thus satisfy these conditions.

[41] Perturbations to the flow field will lead to harmonic meandering instabilities on the timescale of melting. The linear contribution to this balance governs the amplification of perturbations to the channel centerline, while the zeroth order contribution is lateral migration in the unperturbed state. The channel width is assumed to be fixed

$$y_b|_{n=\pm 1} = y_c \pm 1, \quad (50)$$

and we also assume that the zeroth-order lateral migration is balanced by glacial surface lowering so that  $dS^*/dt^* = dh_0^*/dt^*$ . At linear order, however, equation (23) becomes (evaluated at the outside of the meandering bend)

$$1/C_b = \mathcal{H}_1(1) - \mathcal{D}_1(1). \quad (51)$$

Equation (51) provides an implicit dispersion relation between  $\omega$  and  $\lambda_m$  for acceptable growth rate amplitudes (the real part of  $i\omega$ ) and propagation velocities (the imaginary part of  $i\omega$ ) of harmonic channel perturbations.

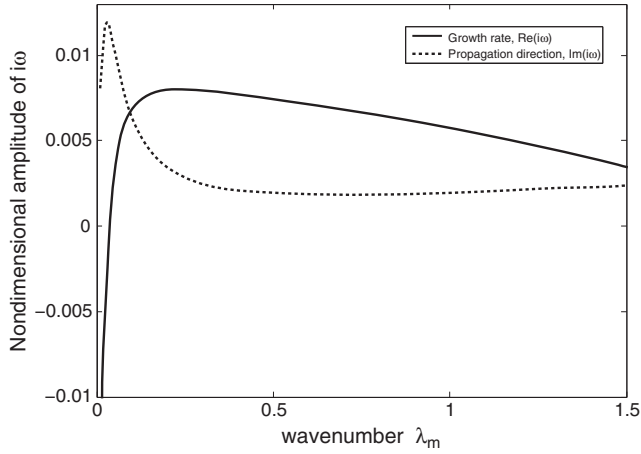


**Figure 3.** Solution to the dispersion relation equation (51) as a function of wave number  $\lambda_m$  for  $U_0^* = 1$  m/s,  $B_0^* = 0.5$  m,  $D_0^* = 0.2$  m,  $\mathcal{J}^* = 10^{-4}$  s/m,  $\Delta T_G^* = 0.025^\circ\text{C}$ ,  $C^* = 0.1$  W/m<sup>2</sup> K,  $C_b = 0.25$ . Solid curve (real part of  $i\omega$ ) shows that growth rate of perturbations has a single maximum wave number, while dashed curve (imaginary part of  $i\omega$ ) shows downstream meander propagation.

## 5. Results

[42] A typical solution to the dispersion relation equation (49) is given in Figure 3, in which we see that the plotted most unstable wave number also exhibits downstream propagation (imaginary part of  $i\omega$  is positive) with growth rates similar to the propagation speed (real and imaginary parts of  $i\omega$  are similar magnitude). Both downstream and upstream meander propagation occur in our model, although the parameter space of realistic flow variables exhibits downstream propagation. We explore the behavior of the dispersion relation by varying flow variables, channel aspect ratio, and adjustable constants in the governing equations.

[43] We find that for a range of realistic parameters (Table 2), channel bank perturbations are unstable with a maximum wave number, indicating a fastest-growing mode.

The parameter dependencies of this most unstable wave number are shown in Figure 4, plotting the dimensional wavelength ( $2\pi/\lambda_m^*$ ) as a function of control parameters in the problem. The channel aspect ratio  $\beta$  generally exerts greatest control on meander wavelength, and Figure 4 compares the effect of control parameters  $\text{Fr}$ ,  $\Pi_1$  and  $\Pi_4$  with  $\beta$ . Parameter  $\Pi_2$  is generally small compared to other thermal parameters in the parameter range of interest, and  $\Pi_3$  does not enter the  $\mathcal{O}(\varepsilon^1)$  solution. In Figure 4, we take  $\Delta T_G^* = 0.025^\circ\text{C}$  (making the role of conductive heat losses small—this is chosen to match field data, see section 6),  $\mathcal{J}^* = 10^{-4}$  s/m,  $C^* = 0.1$  W/m<sup>2</sup> K, channel half width  $B^* = 0.5$  m, and all other parameters as in Table 2.

[44] We see that meander wavelength varies by about a factor of 10 for the range of parameters considered, including a range of wavelengths ( $2\pi/\lambda_m^* = (8.014 \pm 0.517)2B_0^*$ ) that is consistent with observed meander wavelengths (gray shading, see section 6). Increasing  $\beta$  generally decreases meander wavelength, while increasing the Froude number decreases the wavelength (Figure 4a). At low Froude number, perturbations are stable (real part of  $i\omega < 0$ ) indicating no meandering. The transition from stable to unstable perturbations has a weak dependence on aspect ratio  $\beta$ . The transition to meandering occurs around  $\text{Fr} \sim 0.2$  for  $\beta \sim 1$  and around  $\text{Fr} \sim 0.4$  for  $\beta \sim 5$ .  $\Pi_1$  (increasing dissipation relative to temperature advection toward boundaries) and  $\Pi_4$  (coupling to lateral boundary migration) have generally weak influence on meander wavelength, but in both cases a transition to no meandering occurs as these parameters increase (Figure 4b).

[45] We also explore the effect of varying adjustable constants  $\mathcal{J}^*$ ,  $C^*$ ,  $C_b$  and water temperature difference  $\Delta T_G^*$  (Figure 5). Meander wavelength generally increases with increasing  $\Delta T_G^*$ , although the dependence diminishes for large temperature differences and the hydraulic parameters considered ( $U_0^* = 0.5 - 1.5$  m/s,  $D_0^* = 0.2$  m,  $B_0^* = 0.5$  m,  $\mathcal{J}^* = 10^{-4}$  s/m,  $C^* = 0.1$  W/m<sup>2</sup> K in Figure 5a). At low velocities, increasing  $\Delta T_G^*$  can make perturbations stable and shut off meandering. Meander wavelength increases with  $\mathcal{J}^*$  (Figure 5b, fixing  $\Delta T_G^* = 0.025^\circ\text{C}$ ). Coupling constant  $C^*$

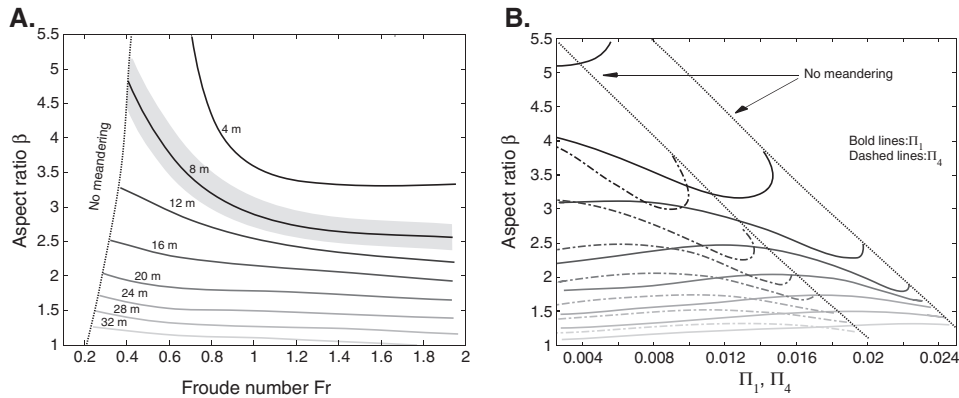


**Figure 4.** Regime diagram for the parameter ranges in Table 1 with  $B_0^* = 0.5$  m, contouring dimensional wavelength ( $2\pi/\lambda_m^*$ , numbered) as a function of (a) Froude number  $\text{Fr}$  versus aspect ratio  $\beta$ , with gray bar illustrating the range of wavelengths that are consistent with natural meanders. (b)  $\Pi_1$ ,  $\Pi_4$  versus aspect ratio  $\beta$ . Dashed lines correspond to  $\Pi_4$  while solid lines correspond to  $\Pi_1$  in the same range. The dotted lines in both panels signify a transition to stable perturbations (no meander formation). Downstream meander propagation occurs for all parameter choices in this figure.

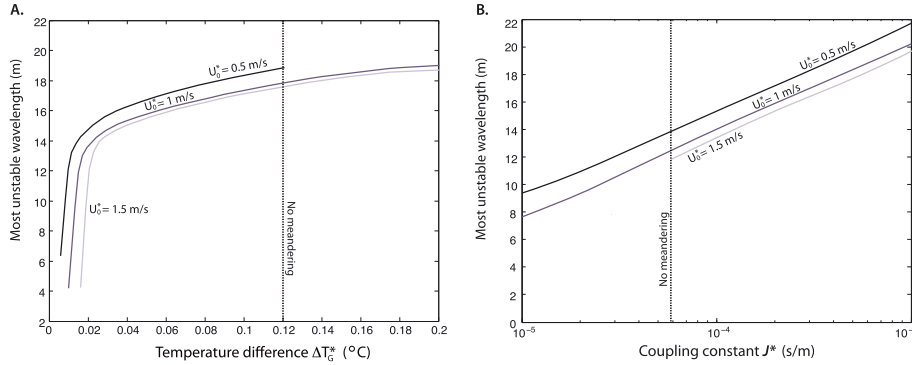


**Figure 5.** Effect on dimensional meander wavelength  $2\pi/\lambda_m^*$  of varying (a) bulk temperature difference  $\Delta T_G^*$  and (b) coupling constant  $J^*$  for temperature field advection. Curves vary the characteristic velocity scale  $U_0^*$ . Dotted lines signify the transition to stable perturbations for  $U_0^* = 0.5$  m/s in Figure 5a and for  $U_0^* = 1.5$  m/s in Figure 5b. Parameters not listed are the same as in Figure 3.

and ratio of lateral to vertical heat transfer  $C_b$  do not affect predicted meander wavelengths more than 5% for the range of parameters explored here (Table 2).

## 6. Discussion

[46] In our model, the origin of meandering in supraglacial channels is an instability driven by channel curvature that enhances heat transfer (hence melting) along the outside of bends. The meander wavelength and amplitude are modulated by the glacier’s surface slope which sets the total potential energy available for flow, a result suggested by some field studies [e.g., *Ferguson, 1973*]. Flow variables in general are not independent: A surface energy balance connects solar radiation to total available meltwater flux and thus flow speed, water temperature, and channel aspect ratio. Channel geometry does not remain static in supraglacial streams, and coevolves with variable solar forcing. We do not address these complexities but rather identify a range of flow conditions for which meandering can occur.

[47] However, even in the context of this parameter study, it is interesting to compare model results with field data. Detailed hydraulic parameters are poorly constrained in general for supraglacial streams, but there are a number of studies that provide meander wavelengths and channel widths [*Leopold and Wolman, 1960; Parker, 1975; Knighton, 1981; Marston, 1983*]. We have compiled these meander wavelength and channel width data and collected additional data from the Juneau Icefield and from IKONOS satellite photos (July 2007) of the West Greenland Icesheet. These data are plotted in Figure 6 and show a power law relationship between channel width and meander wavelength for supraglacial streams over three orders of magnitude in channel width (Figure 6). Such behavior is consistent with the power law channel width versus meander wavelength relationship also found for alluvial and bedrock meanders. Although the coefficients of these empirical relations appear to differ by up to an order of magnitude as the composition of the erodible substrate varies [*Leopold et al., 1964*], the power does not differ and remains similar to unity.

[48] The paucity of available data on supraglacial streams makes it premature to evaluate the significance of the data in Figure 6 in the context of other meandering systems.

A direct comparison between our model and the observed supraglacial channel widths and wavelengths seen in the field is also not attempted here, as the covariance of flow parameters (the hydraulic geometry and slope variations) for supraglacial streams is not yet well constrained. However, we can find a range of parameters (Figure 4a, gray bar) that are consistent with conditions often found in natural channels and that reproduce the empirical scaling between channel width and supraglacial meander wavelength in Figure 6. We find that it is necessary to choose a low temperature difference between stream water and boundary ice to generate meandering wavelengths that match field data ( $\Delta T_G^*$  less than  $0.05^\circ\text{C}$ , Figure 5a). Because water temperature is strongly buffered toward zero in these systems, such small temperature differences may be reasonable. However, it is also possible that higher order effects on the curvature-induced redistribution of heat within the stream (e.g., secondary current not modeled here [*Seminara, 2006*]) may be important for the details of realistic meander wavelength prediction. We expect that a more complete treatment of variable glacier surface energy balance and of flow within the stream may better constrain the temporal evolution of meanders. However, the present model appears satisfactory in predicting the onset of lateral channel instabilities.

[49] Agreement between modeled and observed meander wavelength/width scaling allows us to constrain the mechanisms for meander formation in supraglacial streams (relative magnitude of forcing terms for model solutions that overlap with observations). The gray bar in Figure 4 shows that meanders form when flow is slightly subcritical to supercritical ( $Fr > \sim 0.4$ ) with channel aspect ratios  $\beta \sim 2.5 - 5$ . Comparing the relative magnitudes of the thermal control parameters, we see that the advective terms  $\Pi_1, \Pi_4$  likely dominate conductive losses through ice ( $\Pi_2$ ) when balanced against dissipation. Thus, the enhanced heat production through dissipation and increased lateral heat transfer induced by curvature are the primary thermal drivers of meandering.

[50] The present model differs from previous modeling by *Parker [1975]* in two important aspects. First, we find that meanders migrate downstream, consistent with our field observations and those of others [*Marston, 1983*]. Second, we find that meanders also occur for subcritical flow

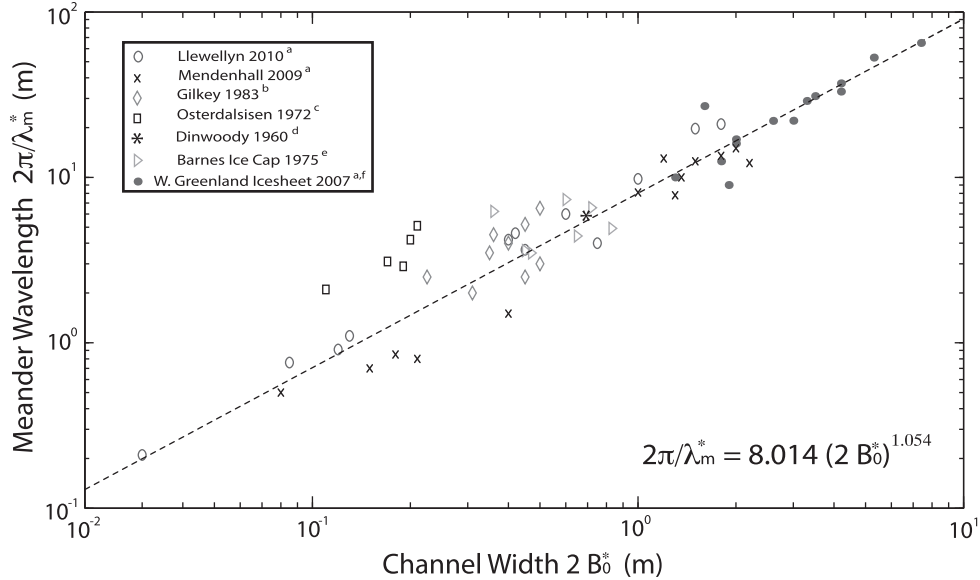


**Figure 6.** Compilation of supraglacial stream channel width versus meander wavelength derived from field studies, using the Levenberg-Marquardt algorithm for the power law fit. Standard error in the intercept is 0.517 and for the exponent is 0.043. Data sources: a. Authors’ measurements; b. *Marston* [1983]; c. *Knighton* [1981]; d. *Leopold and Wolman* [1960]; e. *Parker* [1975]; f. pixel counting IKONOS 1 m resolution satellite images, taken July 2007.

( $Fr < 1$ ). Neither of these conditions were predicted by the linear stability analysis of *Parker* [1975], which did not solve explicitly for the stream velocity field or account for the effects of channel curvature on flow. Thus, as in alluvial meanders [*Seminara*, 2006], consideration of the coupling between evolving channel geometry and the stream flow field appears to be an important aspect of modeling supraglacial stream morphodynamics.

[51] The rate for meander development may be estimated from our model through the growth rate of linear perturbations. For the range of parameters listed in Table 1, we find maximum growth rates in range of 1–10 mm/h. Despite the implicit neglect of time-dependent forcing in this estimate, this is roughly consistent with measured maximum supraglacial stream incision rates of several centimeters per day [*Marston*, 1983] in warm temperate setting where total yearly lowering of the ablation zone may exceed 10 m (E. Hood, personal communication, 2013). Such rapid incision raises the possibility that the drainage network as well as the planform geometry of supraglacial streams may evolve significantly over the course of one melt season. While there are limited data suggesting that this does occur on multiyear timescales [*Leopold and Wolman*, 1960], intraseason reorganization of the supraglacial network could also occur. In the context of high volume systems such as on the Greenland ice sheet, this dynamic reorganization interacts with englacial and subglacial meltwater routing through the drainage of supraglacial lakes [*Box and Ski*, 2007], which may affect the large-scale dynamics of ice sheet movement [*der Wal et al.*, 2008].

[52] Predicted depth perturbations are antisymmetric with respect to the channel centerline, deepening on the outside edges of bends and shallowing on the insides. It is the addition of background lowering of the channel from solar

forcing that sets the balance between lateral and vertical incision. Channel depth below the glacier surface in our model is set by the difference between surface lowering rate and the zeroth-order stream lowering rate  $dS^*/dt^* - dh_0^*/dt^*$  arising from equation (23). This difference may generally be a small negative quantity (net lowering), due to dissipation of heat in the stream and albedo differences between water and ice. Although we anticipate that in some cases (for example, warm rainwater input), significant deepening of channels below the surface may occur [*Jarosch and Gudmundsson*, 2012], in the present study we neglect the relative incision of channels with respect to the surface. For  $\gamma\Delta T_a$  in the range of  $\sim 100$ – $500$  W/m<sup>2</sup> as the solar forcing for stream incision, perturbed lateral migration rates are proportional to vertical incision perturbations through equation (23), and equation (33) predicts lowering at rates similar to migration speeds. This is consistent with the observation of approximately constant channel width in supraglacial streams. However, we do not rule out that variable absorbed solar radiation and a time-varying energy balance are reflected in downstream variations that do exist in channel width.

[53] Supraglacial streams are distinct from other meandering fluvial channels in several important ways. First, the instability driving lateral channel migration is thermal rather than mechanical, such that hydrodynamics in the stream are coupled to bank erosion through forced spatial variations in heat flux at the channel wall. This is fundamentally different than the coupling of hydrodynamics to erosion through sediment transport that occurs in alluvial settings, although it may be more similar to dissolution meanders in Karst settings [*Ford and Williams*, 2007].

[54] A distinctive feature of supraglacial streams is that the discharge is strongly diurnal, especially for streams in which rain or other stored meltwater does not constitute

a large fraction of the total water mass. A supraglacial stream will experience a smoothly varying hydrograph each day, with the same period but slightly out of phase with solar forcing [Marston, 1983]. To attain a regular sinusoidal meandering planform, then, would imply that this pattern is either set early on or is set by the average daily maximum discharge. We believe that the latter case is more likely, because the timescale over which meanders adjust their planform geometry is rapid [Marston, 1983]. We also note that meander wavelengths are not generally constant over the full length of a reach (e.g., Figure 1a). The parameter study here predicts that as increasing slope increases average streamwise velocities, dominant meander wavelengths will get smaller. However, the regime diagram of Figure 4a suggests that all else constant, the velocity dependence of meander wavelength becomes negligible for high velocity flows.

[55] Supraglacial channels represent a mechanistic end member in the spectrum of natural channelization features that exhibit meandering (only thermal erosion), which also includes lava tubes and flows, alluvial rivers, and dissolution channels. A metric relating supraglacial channel morphology to the rates and mechanisms of incision would be a useful remote means of monitoring seasonal meltwater routing on ice sheets, but may be applicable in a much broader planetary context as well. On Earth, it has been suggested that sinuosity of bedrock channels varies as a function of underlying geology and may contain a climate signature [Stark et al., 2010]. Some sinuous channels on Mars record meandering lava flows, as they do on the Moon [Hauber et al., 2009], but others may record fluvial activity from a wetter period of Martian history [Malin and Edgett, 2003]. On Titan, present-day cycling of liquid methane is likely responsible for meandering channels on the icy surface [Lunine and Atreya, 2008], but the rates and mechanisms of incision are currently unknown. The work here proposes mechanistic controls on meandering for thermally eroded supraglacial streams. If it is possible to separate the dominant scales of thermally eroded meanders from those formed through mechanical erosion (for example, through the large intercept of the relationship between width and meander wavelength in alluvial rivers [Leopold and Wolman, 1960]), this can be used to better understand landscape evolution on terrestrial planets and moons in our solar system that exhibit sinuous channels.

[56] **Acknowledgments.** William E. Dietrich and Timothy Creyts are acknowledged for helpful discussions, while Eran Hood, NorthStar Trekking, and the Juneau Icefield Research Program provided logistical support for field work. We thank Jason Box and Geoeye to Impossible Pictures UK for the kind donation of IKONOS imagery of the west Greenland ice sheet. We thank two anonymous reviews and an Associate Editor for formal reviews, and Alice Thompson for checking the math. This research was funded by a graduate student grant from the Geological Society of America, the UC Berkeley Behrman fund, and NASA grant NNX09AN18G.

## References

- Blondeaux, P., and G. Seminara (1985), A unified bar-bend theory of river meanders, *J. Fluid Mech.*, *157*, 449–470.
- Box, J. E., and K. Ski (2007), Remote sounding of greenland supraglacial melt lakes and implications for subglacial hydraulics, *J. Glaciol.*, *53*(181), 257–265.
- Callander, R. A. (1969), Instability and river channels, *J. Fluid Mech.*, *36*(3), 465–480.
- Camporeale, C., P. Perona, A. Porporato, and L. Ridolfi (2007), Hierarchy of models for meandering rivers and related morphodynamic processes, *Rev. Geophys.*, *45*, RG1001. doi:10.1029/2005RG000185.
- Colebrook, C. F. (1939), Turbulent flow in pipes, with particular reference to the transition between smooth and rough pipe laws, *J. Inst. Civ. Eng.*, *11*(4), 133–156.
- der Wal, R. S. W. V., W. Boot, M. R. van den Broeke, C. J. P. P. Smeets, C. H. Reijmer, J. J. A. Donker, and J. Oerlemans (2008), Large and rapid melt-induced velocity changes in the ablation zone of the Greenland ice sheet, *Science*, *321*, 111–113.
- Ferguson, R. I. (1973), Sinuosity of supraglacial streams, *Geol. Soc. Am. Bull.*, *84*, 251–256.
- Ford, D. C., and P. Williams (2007), *Karst Hydrogeology and Geomorphology*, John Wiley and Sons, London.
- Fountain, A. G., and J. S. Walder (1998), Water flow through temperature glaciers, *Rev. Geophys.*, *36*(3), 299–328.
- Hauber, E., J. Bleacher, K. Gwinner, D. Williams, and R. Greeley (2009), The topography and morphology of low shields and associated landforms of plains volcanism in the Tharsis region of Mars, *J. Volcanol. Geotherm. Res.*, *185*, 69–95.
- Ikeda, S., G. Parker, and K. Sawai (1981), Bend theory of river meanders. Part 1. Linear development, *J. Fluid Mech.*, *112*, 363–377.
- Isenko, E., R. Narus, and B. Mavlyudov (2005), Water temperature in englacial and supraglacial channels: Change along the flow and contribution to ice melting on the channel wall, *Cold Reg. Sci. Technol.*, *42*, 53–62.
- Jarosch, A., and M. Gudmundsson (2012), A numerical model for meltwater channel evolution in glaciers, *The Cryosphere*, *6*, 493–503.
- Johannesson, H., and G. Parker (1989), Linear theory of river meanders, in *River Meandering*, vol. 12, edited by S. Ikeda and G. Parker, pp. 181–214, AGU, Washington D. C.
- Knighton, A. D. (1981), Channel form and flow characteristics of supraglacial streams, Austre Okstindbreen, Norway, *Arct. Alp. Res.*, *13*(3), 295–306.
- Leopold, L. B., and M. G. Wolman (1960), River meanders, *Geol. Soc. Am. Bull.*, *71*, 769–793.
- Leopold, L. B., M. G. Wolman, and J. P. Miller (1964), *Fluvial Processes in Geomorphology*, W. H. Freeman and Company, San Francisco.
- Lunine, J., and S. K. Atreya (2008), The methane cycle on Titan, *Nat. Geosci.*, *1*, 159–164.
- Malin, M. C., and K. S. Edgett (2003), Evidence for persistent flow and aqueous sedimentation on early Mars, *Science*, *302*, 1931–1934.
- Marston, R. A. (1983), Supraglacial stream dynamics on the Juneau ice field, *Ann. Assoc. Am. Geogr.*, *73*(4), 597–608.
- Mullins, W. W., and R. F. Sekerka (1963), Morphological stability of a particle growing by diffusion of heat, *J. Appl. Phys.*, *34*, 323–328.
- Parker, G. (1975), Meandering of supraglacial melt streams, *Water Resour. Res.*, *11*(4), 551–552.
- Schlichting, H. (1960), *Boundary Layer Theory*, 4th ed., McGraw-Hill Book Company, London.
- Seminara, G. (2006), Meanders, *J. Fluid Mech.*, *554*, 271–297.
- Seminara, G., and M. Tubino (1992), Weakly nonlinear theory of regular meanders, *J. Fluid Mech.*, *244*, 257–288.
- Sklar, L. S., and W. E. Dietrich (2004), A mechanistic model for river incision into bedrock by saltating bedload, *Water Resour. Res.*, *40*, W06301. doi:10.1029/2003WR002496.
- Smith, J. D., and S. R. McLean (1984), A model for flow in meandering streams, *Water Resour. Res.*, *20*(9), 1301–1315.
- Stark, C. P., J. R. Barbour, Y. S. Hayakawa, T. Hattanji, N. Hovius, H. Chen, C.-W. Lin, M.-J. Horng, K.-Q. Xu, and Y. Fukahata (2010), The climatic signature of incised river meanders, *Science*, *327*, 1497–1500.